Diagnosis of Melanoma with ^{61}Cu-Labelled PET Tracer

Szilvia Bunda,[a] Ibolya Kálmán-Szabó,[b,c] Norbert Lihi,[d]* Zita Képes,[b] Dezső Szikra,[b] Judit Peline Szabo,[b] István Tímári,[e,f] Dániel Szücs,[b] Nóra V. May,[g] Gábor Papp,[a] György Trencsényi[b,c] and Ferenc K. Kálmán[a]*

[a)] Department of Physical Chemistry, University of Debrecen, H-4032 Debrecen, Egyetem tér 1., Hungary, E-mail: kalman.ferenc@science.unideb.hu

[b)] Division of Nuclear Medicine and Translational Imaging, Department of Medical Imaging, University of Debrecen, H-4032 Debrecen, Egyetem tér 1, Hungary

[c)] Gyula Petrányi Doctoral School of Clinical Immunology and Allergology, Faculty of Medicine, University of Debrecen, Nagyerdei St. 98, H-4032, Debrecen, Hungary

[d)] HUN-REN–UD Mechanisms of Complex Homogeneous and Heterogeneous Chemical Reactions Research Group, Department of Inorganic and Analytical Chemistry, University of Debrecen, H-4032 Debrecen, Egyetem tér 1, Hungary, E-mail: lihi.norbert@science.unideb.hu

[e)] Department of Organic Chemistry, University of Debrecen, H-4032 Debrecen, Egyetem tér 1, Hungary

[f)] HUN-REN-UD Molecular Recognition and Interaction Research Group, University of Debrecen, H-4032 Debrecen, Egyetem tér 1, Hungary

[g)] Centre for Structural Science, Research Centre for Natural Sciences, Hungarian Research Network (HUN-REN), Magyar tudósok körútja 2, H-1117 Budapest, Hungary

Abstract

Until the recent years, substances containing radioactive ^{61}Cu were strongly considered as potential positron emitting radiopharmaceuticals to be used in PET applications, however due to its suitably long half-life, generator independent and cost-effective production, those seem to be economically viable for human imaging. Since, the malignant melanoma is a major public health problem, its early diagnosis is a crucial contributor to the long-term survival, which can be achieved by radio labelled alpha-melanocyte-stimulating hormone analog NAPamide derivatives. Here, we report on the physico-chemical features of a new CB-15aneN$_5$-based Cu(II) complex ([Cu(KFTGdiac)]$^-$) and the *ex vivo* and *in vivo* characterization of its NAPamide conjugate. The rigid chelate possesses prompt complex formation and suitable inertness ($t_{1/2}$ = 18.4 min in 5.0 M HCl at 50 °C) as well as excellent features in the diagnostics

of B16-F10 melanoma tumors (T/M(SUVs) (*in vivo)*: 12.7, %ID/g: 6.6 ± 0.3, T/M (*ex vivo*): 22).

1. Introduction

Considering the rising pervasiveness of malignant melanoma (MM) and its strong propensity to metastasize, timely disease diagnostics is emerging as a central issue in current health sciences.[1] To this end, the interest in the development of target specific imaging probes is steadily increasing. In nuclear medical settings, a diverse array of radiolabelled MM-targeting vectors including melanin-associated benzamide compounds (BZA), monoclonal antibodies (MoAb) and nanoparticles has been constructed for the positron emission tomography (PET) and single-photon emission computed tomography (SPECT)-based identification of primary MM and related metastases.[2–7]

Seven-pass transmembrane G-protein coupled melanocortin-1 receptor (MC1-R) is a central biomarker of MM abundantly expressed on the surface of the majority of melanoma tumor cells.[8–10] Upon being stimulated by α-melanocyte-stimulating hormone (α-MSH/(Ac-SYSMEHFRWGKPV-NH_2), MC1-R activates downstream signalling pathways of pigmentation, melanin synthesis and cell proliferation.[2,11] Hence, given the overexpression of MC1-R on MM, α-MSH and its analogues seem to be strong applicants for the development of MM selective peptide radiopharmaceuticals. Earlier preclinical findings capitalize on the relevance of radiolabelled α-MSH analogue NAPamide as attractive ligands for the peptide-based molecular imaging of MM.[12–14]

Beyond the most frequently applied NAPamide molecule however, other α-MSH analogues including HOLDamide, FOLDamide, and MARSamide have also been recently established as valuable tools in MC1-R positive (MC1-R pos.) experimental MM imaging.[15]

To date, a wide variety of radiometals were used and proved to be feasible in the radiolabelling of NAPamide derivatives for MC1-R expressing melanoma tumor imaging including Copper-64 (^{64}Cu), Gallium-68 (^{68}Ga), Fluorine-18 (^{18}F), Indium-111 (^{111}In), Scandium-44 (^{44}Sc) and Technetium-99 m ($^{99\,m}$Tc).[12–14,16] More recently, increasing attention has been placed upon the use of Copper-61 (^{61}Cu) for PET diagnostic applications.[17] Due to its suitably long half-life ($t_{1/2}$: 3.32 hours) and generator independent production, the application of ^{61}Cu (β^+ emission: 1159 keV, 61% β^+, E_{max} = 1.216 MeV, γ emission: 511 keV) seems to be economically viable for PET imaging purposes.[18,19] Moreover, the favourable physicochemical properties along with the long-lived nature of ^{61}Cu, allows for the covering of extended imaging

periods and for the seamless adjustment of the radionuclide to molecules with longer pharmacokinetics. In a practical sense - *given the long decay half-life* - the radioisotope or the ^{61}Cu-labbelled radiopharmaceuticals can be easily shipped for PET imaging studies to remote facilities without on-site cyclotron.[20,21] The features mentioned above collectively make ^{61}Cu an excellent candidate for PET applications. Besides the radiometal, however, the choice of the most appropriate chelator is also of utmost importance to optimize the pharmacokinetics and the imaging characteristics of the radiotracers. In our previous study chelator KFTG (4-(1,4,7,10,13-pentaazabicyclo[8.5.2]heptadecan-13-ylmethyl)benzoic acid) - *belonging to the CB-15aneN$_5$ (1,4,7,10,13-pentaazabicyclo[8.5.2]heptadecane) ligand family* - was constructed for complexation with ^{61}Cu(II), and displayed excellent complex formation capability ($t_{1/2}$ = 155 s at pH 5.0 and 25 °C), outstanding physicochemical inertness ($t_{1/2}$ = 2.0 h in 5.0 M HCl at 50 °C) and moderate superoxide dismutase activity (IC_{50} = 2.3 μM) based on the xanthine/xanthine oxidase/NBT assay.[17] Furthermore, the results of the microPET acquisition and the post imaging biodistribution render [^{61}Cu]Cu-KFTG-NAPamide meaningful attractiveness for the imaging of MC1-R overexpressing melanoma tumors.

Initiated by these prior observations, we intended to assess the influence of the addition of two acetate (-CH_2-COOH) groups to KFTG on the radiochemical synthesis, physicochemical properties, and the *in vivo* behaviour of this new chelator (KFTG-diac (2,2'-(13-(4-carboxybenzyl)-1,4,7,10,13-pentaazabicyclo[8.5.2]heptadecane-4,7-diyl)diacetic acid), Scheme 1.). Thus, in this study we present the synthesis of the KFTGdiac, the formation and dissociation kinetic features of its Cu(II) complex, the structural features of the chelate, the conjugation of the ligand to NAPamide molecule and the radiolabelling of the KFTGdiac-NAPamide conjugate with ^{61}Cu. In addition, we report preliminary results on the *in vitro* biological properties, the *in vivo* tumor-homing potential and imaging behaviour of the newly introduced [^{61}Cu]Cu-KFTGdiac-NAPamide formulation applying MC1-R pos. B16F10 melanoma cell lines, and corresponding C57BL/6 tumor-bearing mice.

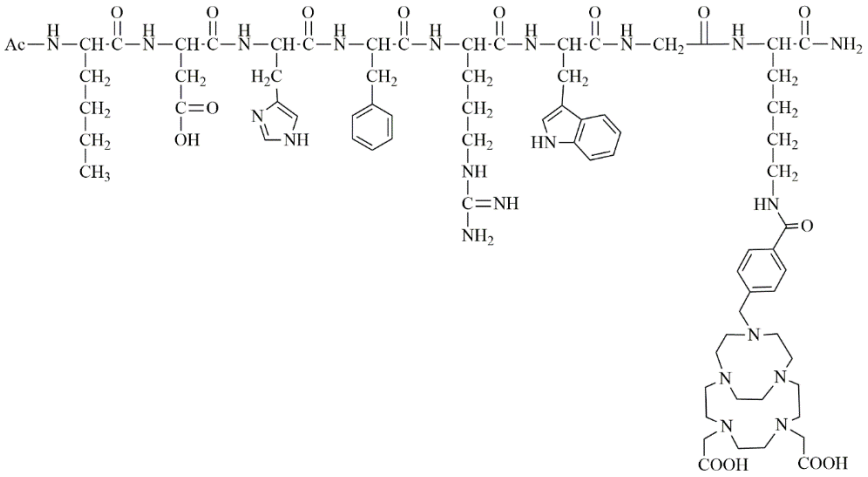

Scheme 1. The structure of the KFTGdiac-NAPamide conjugate.

2. Results and discussion

2.1. Synthesis of the ligand

The KFTG ligand was synthesized according to the procedure published previously by Kálmán-Szabó and her coworkers.[17] The incorporation of the acetate pendants has been carried out by using tert-butyl bromoacetate in ACN (acetonitrile). In the alkylation reaction K_2CO_3 was used as a base to eliminate the HBr by-product. Majority of the *bis*(*t*Bu)-KFTGdiac ((4-((4,7-bis(2-(tert-butoxy)-2-oxoethyl)-1,4,7,10,13-pentaazabicyclo[8.5.2]heptadecan-13-yl)methyl)benzoic acid)) was directly used for biological investigation, while the remained part was deprotected and investigated in kinetic and structural studies. Detailed characterization of the new ligands (Figure S1-S8) is provided in the SI. The synthesis of KFTG-NAPamide was performed by standard amide conjugation, thus *bis*(*t*Bu)-KFTGdiac bifunctional chelator was coupled via an active ester to the free amine group of the lysine unit of the resin-bound NAPamide peptide using HBTU (hexafluorophosphate benzotriazole tetramethyl uronium) and DIPEA (*N*,*N*-diisopropylethylamine) activation strategy. Then, the obtained resin-bound peptide derivative was deprotected and cleaved from the resin with acidic hydrolysis using 95% TFA (trifluoracetic acid). The crude peptide with the KFTG moiety was purified by semipreparative RP-HPLC (reversed-phase high pressure liquid chromatography). The chelator-conjugated NAPamide was identified by HRMS (high-resolution mass spectrometry).

2.2. Kinetic investigations

In order to preserve the diagnostic and therapeutic effects of the radiopharmaceuticals, the fast complexation of the short-lived radioisotopes is essential to minimize radioactive decay.

In most cases, the chelation of the Cu(II) by the rigidified tetraaza-macrocycles requires high temperature and organic solvents which are obviously time and resource consuming.[22] To the best of our knowledge, only the phosphonate derivatives of the cross-bridged tetraaza-tetraazacyclotetradecane, CB-TE2P ((1,4,8,11-tetraazabicyclo[6.6.2]hexadecane-4,11-diylbis(methylene))diphosphonic acid) and CB-TE1A1P (2-(11-(phosphonomethyl)-1,4,8,11-tetraazabicyclo[6.6.2]hexadecan-4-yl)acetic acid), form complexes with Cu(II) ion readily at room temperature.

For this reason, the formation of the $[Cu(KFTGdiac)]^-$ complex was studied according to the method published by our group previously.[17,23] The complex formation reaction was followed in the presence of ligand excess (×10) to ensure pseudo-first-order condition at 25 °C in the pH range 3.0 – 4.4 (Figure 1). In these reactions the rate of the complex formation can be described by the rate equation $d[CuL]_t/dt = k_{obs}[Cu(II)]$, where $[CuL]_t$ is the total concentration of the chelate.

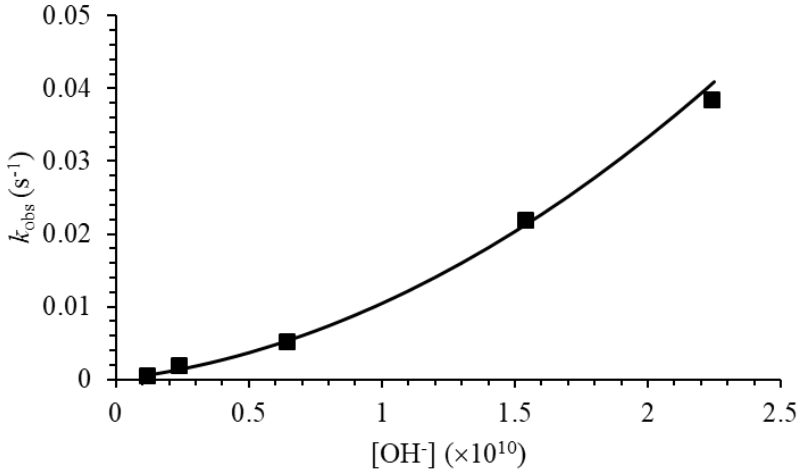

Figure 1. Plot of the first-order rate constants (k_{obs}) as a function of $[OH^-]$ for the formation of $[Cu(KFTGdiac)]^-$ complex (0.15 M NaCl, 25 °C).

As shown in Figure 1, the k_{obs} values obtained at different pH values are directly proportional to the increase of $[OH^-]$ and the rate of complex formation also exhibits second-order dependence on OH^- concentration. This observation suggests that the rate constants obtained can be expressed as follow:

$$k_{obs} = k_1[OH^-] + k_2[OH^-]^2 \quad (1)$$

where k_1 and k_2 are the rate constants characterizing the transformation of the intermediate to product assisted by the OH^-. Fitting of the pseudo-first rate constants to equation (1) delivered values $(4.3 \pm 0.8)\times10^7$ $M^{-1}s^{-1}$ and $(6.2 \pm 1.3)\times10^{17}$ $M^{-2}s^{-1}$ for k_1 and k_2, respectively. For better comparison, the half-life ($t_{1/2} = \ln2/k_{calc}$) of the complex formation was calculated to be 1.1 s at pH = 5.0 which is two orders of magnitude lower than that was obtained for the $[Cu(pNO_2Bn\text{-}CB\text{-}15aneN_5)]^{2+}$ ($t_{1/2}$ = 133 s)[23] and $[Cu(KFTG)]^-$ ($t_{1/2}$ = 155 s)[17] complexes. The results show that the KFTGdiac ligand forms complex with Cu(II) ion in less than 8 sec (circa 7 times $t_{1/2}$) at pH 5.0 and 25 °C. This outstanding behaviour can be explained by considering the formation of a stable intermediate in which the acetate pendants act as anchoring groups. This promotes the binding of nitrogen donor atom(s) of the ligand backbone to copper(II) allowing the easier and faster formation of the "in-cage" complex. The formation of the complex was confirmed by MS (mass spectrometry) measurement (Figure S9).

As it is known, the dechelation process of rigidified Cu(II) complexes is extremely slow under mild conditions, their inertness is usually investigated under harsh circumstances such as high acid concentration and temperature.[24] Due to the extremely slow dissociation of the complexes, the detailed investigation of the dissociation pathways such as proton- and metal-assisted dechelation is not possible under physiological conditions. For this reason, the inertness of the complexes frequently studied at high acid concentration (e.g. 5 M HCl) and elevated temperature (50 or 90 °C). Since the high H^+ concentration ensures the pseudo-first order conditions the k_{obs} values are pseudo-first order rate constants, which can be easily converted to dissociation half-lives for comparative purposes. The inertness of the $[Cu(KFTGdiac)]^-$ was investigated in 5.0 M HCl at 50 °C. The calculated $t_{1/2}$ value (18.4 ± 0.2 min) was found to be more or less the seventh of those obtained for the $[Cu(KFTG)]^-$ (2.0 h)[17] and $[Cu(pNO_2Bn\text{-}CB\text{-}15aneN_5)]^{2+}$ (2.3 h)[23] complexes. It is worth mentioning that the half-life of the dechelation would be 880 years at physiological pH by assuming that further dissociation pathways or enzymatic cleavage processes are not operative. The high inertness is also confirmed by the fact that, we did not observed any release of ^{61}Cu from the [^{61}Cu(KFTGdiac)]-NAPamide tracer in human plasma at 37 °C during 5 hours (*vide infra*).

The results indicate that the incorporation of the acetate pendants (functional group bearing dissociable H^+ ion) promotes the proton transfer to the N-donor atoms of the macrocycle from the pendant, which leads to the liberation of the Cu(II) ion. For the sake of clarity, the features of the complex determined in aqueous solution are only good approximations to describe the properties of the [^{61}Cu(KFTGdiac)]-NAPamide radiopharmacon. Although the inertness of $[Cu(KFTGdiac)]^-$ is lower than that of many cross-

bridged Cu(II) complexes,[25] biological experiments performed with this agent candidate prove that the inertness is high enough for PET diagnostic applications.

The SOD activity of the $[Cu(KFTGdiac)]^-$ complex was tested by using the indirect xanthine/xanthine oxidase/NBT assay. The measured inhibition values as a function of the concentration of $[Cu(KFTGdiac)]^-$ complex are shown in Figure S10. The results clearly show that the $[Cu(KFTGdiac)]^-$ complex does not significantly catalyse the decomposition of superoxide anion in the investigated concentration range, thus the determination of IC_{50} value is not feasible.

2.3. EPR measurements and DFT calculation

EPR (electron paramagnetic resonance) spectroscopy and DFT (density-functional theory) calculations were carried out to study the coordination mode of the $[Cu(KFTGdiac)]^-$ complex. pH dependent EPR spectra recorded in the Cu(II)/ KFTGdiac system are registered at 77 K and the spectra are shown in Figure 2. The frozen solution EPR spectra can be fitted well by considering the formation of two copper(II) complexes (component 1 and component 2). The ratio of these species does not change by increasing the pH, therefore coordination isomers are present in the studied pH range. Simulation of the spectra revealed that component 1 is only a minor species and the large g_z value is consistent with the weaker ligand field around the copper(II) center (Table S3). In this case, the binding of 3 nitrogen atoms is expected in the equatorial plane of copper(II) and the complex features elongated octahedral coordination polyhedron. For component 2, the g_z and A_z values are different from those obtained for $[Cu(CB\text{-}15aneN_5)]^{2+}$ and $[Cu(p NO_2Bn\text{-}CB\text{-}15aneN_5)]^{2+}$ complexes.[23,24] In these complexes, copper(II) coordinates to the ligand via 5 nitrogen donor atoms leading to the formation of square-pyramidal coordination polyhedron. Moreover, spin-Hamiltonian parameters of [Cu(Cyclen)] (cyclen: 1,4,7,10-tetraazacyclododecane) also differ from those of $[Cu(KFTGdiac)]^-$ complex,[26] thus it is excluded that only 4 nitrogen donor atoms are involved in the coordination of copper(II). This leads us to the conclusion that the KFTGdiac ligand binds copper(II) via 4 nitrogen donor atoms and the carboxylate pendant arm(s) may also contribute to the metal binding. However, the binding of the carboxylate pendant does not occur in a regular (90°) arrangement to copper(II). Thus, significant rhombic distortion was observed resulting in large g_z and small A_z values. The geometry of the coordination isomers was further studied by DFT calculations.

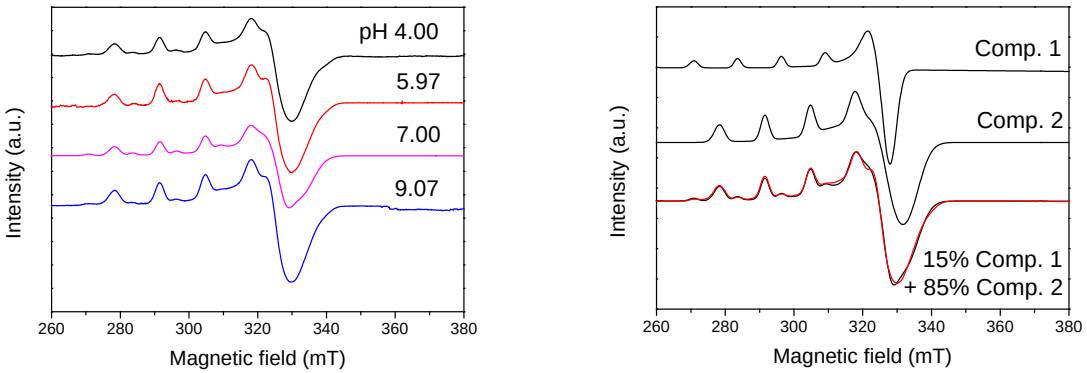

Figure 2. Left panel: pH dependent EPR spectra recorded in the Cu(II) / KFTGdiac system at 77 K, $c_{Cu(II)}$ = 1.71 mM; Right panel: Experimental (black) and simulated (red) EPR spectrum recorded at pH 7.0. The spectrum was fitted with component 1 in 15 % and component 2 with 85 %.

For Component 1, DFT predicted the binding of three nitrogen atoms of the macrocylcle, moreover, the equatorial sphere of the copper(II) is completed by the binding of carboxylate pendant arm (Figure 3). Cartesian coordinates and the corresponding bond lengths are summarized in the SI (Table S4, S5). The calculated EPR parameters are in reasonable agreement with those obtained by the simulation (Table S3). For component 2, it is important to note, that geometry optimization of this complex is not feasible when both carboxylate arms coordinate to copper(II). Thus, we expect the binding of an exclusive carboxylate arm. DFT optimized structure is shown in Figure 3 and the corresponding Cartesian coordinates and bond lengths are reported in Table S4 and S6. DFT calculation revealed indeed a distorted square-pyramidal coordination geometry in which the equatorial plane of copper(II) is accommodated by the 4 nitrogen donor atoms with the average bond length of 2.018 Å and the apical position is completed by the binding of carboxylate arm with the bond length of 2.398 Å. Furthermore, the bond angle of the COO^{-} – Cu(II) – N_{eq} was found to be 75.7° which deviation from the regular 90° may result in significant rhombicity in the EPR parameters. The calculated EPR parameters also confirm the structure of the complex (Table S3).

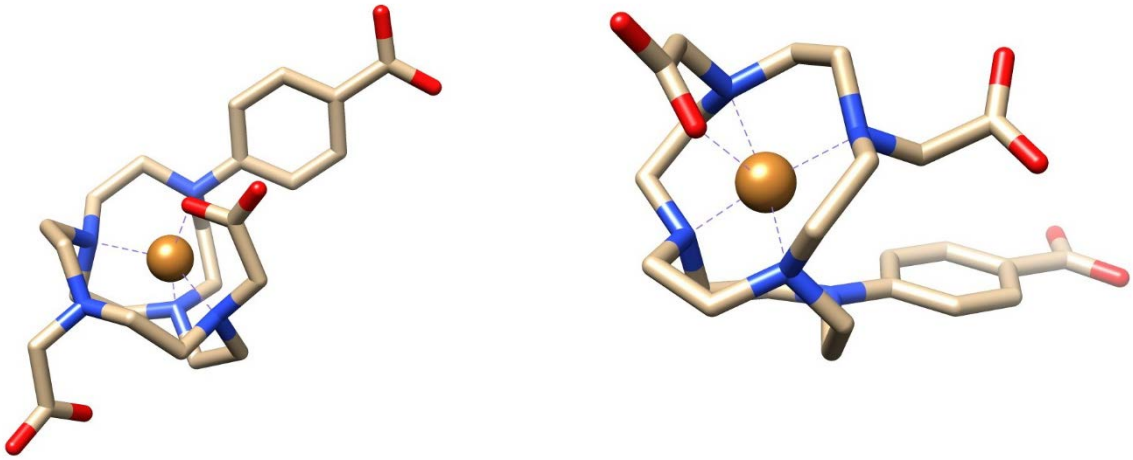

Figure 3. DFT optimized structures of Component 1 (left) and Component 2 (right) formed in the in the Cu(II)/ KFTGdiac system. Hydrogen atoms are omitted for clarity.

2.4. *In vitro* cell experiments

The receptor binding specificity of [^{61}Cu]Cu-KFTGdiac-NAPamide to MC1-R was investigated *in vitro* by comparing its uptake in receptor expressing B16F10 melanoma cells (unblocked) and α-MSH pretreated counterparts (blocked). The *in vitro* data indicated notably higher [^{61}Cu]Cu-KFTGdiac-NAPamide accumulation in the unblocked B16F10 melanoma cells compared to the receptor-blocked ones at all investigated time points ($p < 0.01$), that confirmed the receptor affinity of the radiolabelled probe (Figure 4). In a like manner, the uptake of [^{61}Cu]Cu-KFTG-NAPamide in receptor pos. B16F10 cells was more increased than in amelanotic A375 cells, that implied that the change of the chelator from KFTG to KFTGdiac did not alter the MC1-R binding potential of the radiopharmaceutical.[17] Similarly, former *in vitro* studies presenting higher ^{68}Ga/^{44}Sc-labelled NAPamide accretion in MC1-R overexpressing B16F10 melanoma cells compared to the receptor negative A375 cell line, also verified the MC1-R specificity of the α-MSH analogue.[12]

To further verify the receptor binding specificity and the stability of [^{61}Cu]Cu-KFTGdiac-NAPamide, washout (efflux) investigations were conducted, during which the B16F10 cells were subjected to [^{61}Cu]Cu-KFTGdiac-NAPamide-based treatment and washing rounds, that was followed by a ten-minute-long incubation without radioactivity. In accordance with reports on [^{61}Cu]Cu-KFTG-NAPamide,[17] no significant difference *($p < 0.05$)* was found between the baseline and the post-efflux radioactivity accumulation of the cells (Figure 4), therefore we can conclude that the radiolabelled NAPamide derivative not only shows target selectivity to the melanoma cells, but it also has stable binding, which is of paramount

importance for PET imaging purposes. Nevertheless, with the progress of time a continuous decrease in the radiopharmaceutical accumulation was observed with respective baseline ID% (ID: injected dose) values being 1.14 ± 0.14, 0.98 ± 0.15, 0.75 ± 0.14 and 0.68 ± 0.20 at the 30-, 60-, 90- and 180-min time point (Figure 4). Although, this may indicate the feasibility of the probe for early imaging, in order to cover extended imaging periods, further structural or chemical modifications need to be considered.

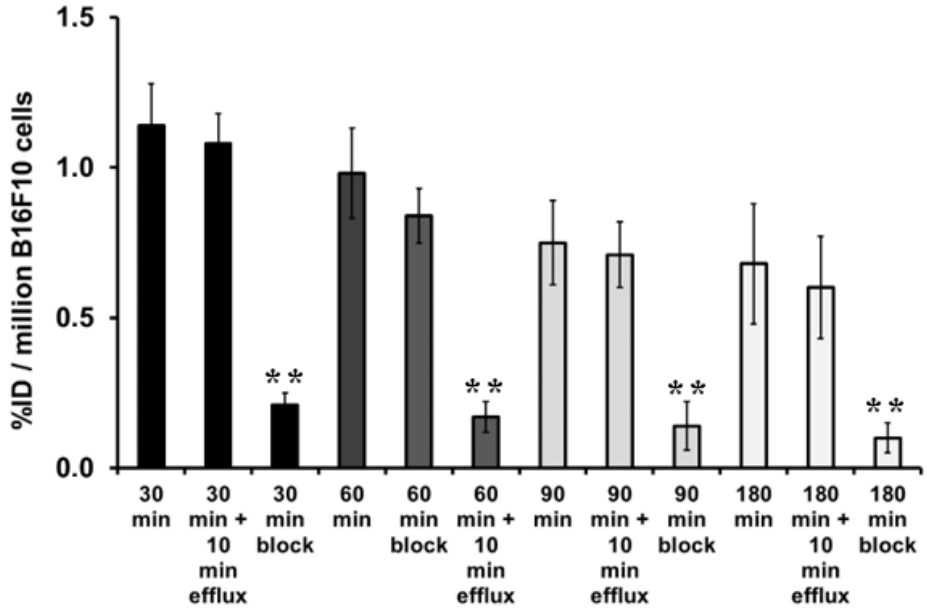

Figure 4. Assessment of time dependent *in vitro* cellular uptake, efflux and blocking studies of the MC1-R specific [^{61}Cu]Cu-KFTGdiac-NAPamide using receptor pos. B16F10 cells. Data shown as mean ± SD (SD: standard deviation). [^{61}Cu]Cu-KFTGdiac-NAPamide accumulation in 10^6 cells was expressed as the percentage of the incubating dose (ID%). Significance level: $p \leq 0.01$ (**).

2.5. *In vivo* miniPET imaging

Using melanoma tumor model, i*n vivo* preclinical PET imaging was accomplished to determine the MC1-R pos. tumor targeting capability and the organ uptake of [^{61}Cu]Cu-KFTGdiac-NAPamide. Given that mouse-derived B16F10 melanoma tumor cells exhibit more than 20,000 MC1-R, experimental B16F10 melanoma models are well-suited for the characterisation of the *in vivo* imaging behaviour of MC1-R targeting diagnostic probes.[14]

The radiopharmaceutical uptake of the B16F10 tumors on [^{61}Cu]Cu-KFTGdiac-NAPamide PET is demonstrated in Figure 5. Analysing the decay-corrected PET scans, the B16F10 tumors could be well delineated from the background at all investigated time points

that confirmed the MC1-R pos. tumor targeting potential of the newly constructed PET probe (Figure 5, Panel A, red arrows).

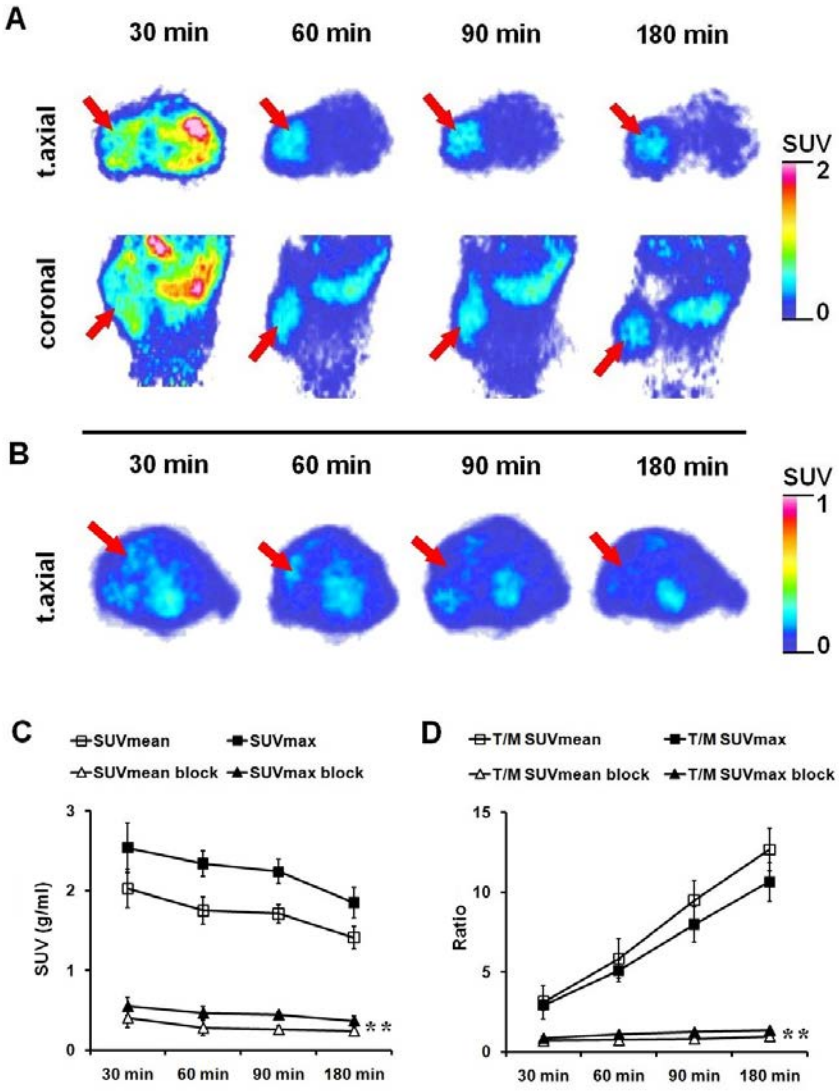

Figure 5. *In vivo* [^{61}Cu]Cu-labeled KFTGdiac-NAPamide miniPET imaging and quantitative image analysis of MC1-R pos. B16F10 melanoma tumors. Static transaxial and coronal (**Panel A**) PET imaging of B16F10 melanoma tumors 30, 60, 90 and 180 min post injection of [^{61}Cu]Cu-KFTGdiac-NAPamide. Representative transaxial PET images of α-MSH blocked *(see Materials and Methods section)* MC1-R pos. B16F10 tumors in C57BL/6 mouse (**Panel B**). Quantitative SUV (standardized uptake value) analysis of [^{61}Cu]Cu-KFTGdiac-NAPamide accumulation in experimental melanoma tumors (**Panel C** and **D**). The decay-corrected PET images and data were obtained 9 ± 1 days after tumor cell inoculation. n = 5 animals/time point. Red arrows: B16F10 tumors. SUV values are presented as mean ± SD. Significance level between the baseline and the blocked data: $p \leq 0.01$ (**).

Previous preliminary screening of ^{61}Cu-labelled NAPamide radiotracer with the same chelator lacking in the acetate groups ([^{61}Cu]Cu-KFTG-NAPamide) also showed outstanding MC1-R pos. tumor-homing ability.[17] Hence, it seems that the modification of the chemical structure of chelator KFTG (the addition of extra acetate groups) has no significant effect on the MC1-R binding ability of the radiotracer. Furthermore, consistent with our findings, higher uptake of radiolabelled α-MSH analogues was reported in receptor expressing experimental B16F10 tumors than in A375 tumors with negligible MC1-R presence.[27–29] Accordingly, NAPamide compounds labelled with ^{64}Cu, - ^{18}F, - ^{44}Sc, - and ^{68}Ga also showed selective MC1-R binding affinity and tumor-homing.[12,14,16,30] Besides NAPamide containing radiotracers, radiolabelled α-MSH analogue HOLDamide seemed to be a strong applicant for MC1-R pos. tumor imaging as well.[30]

The lack of radiotracer uptake during the blocking experiments further strengthened the target specificity of [^{61}Cu]Cu-KFTGdiac-NAPamide (Figure 5, Panel B, red arrows).

The quantitative assessment of [^{61}Cu]Cu-KFTGdiac-NAPamide is presented in Figure 4, Panel C and D. The SUV_{mean} of the tumor on the static images were 2.03 ± 0.24, 1.75 ± 0.17, 1.71 ± 0.12 and 1.41 ± 0.14 at the 30th, 60th, 90th and 180th minute time points; respectively, while the SUV_{max} values were as follows at the same measurement times: 2.54 ± 0.31, 2.34 ± 0.16, 2.24 ± 0.15 and 1.85 ± 0.19. In line with the visual analysis, the tumor uptake of the radioactivity gradually declined from the 30th minute post-injection (SUV_{mean}: 2.03 ± 0.24; SUV_{max}: 2.54 ± 0.31) until the end of the examination (SUV_{mean} at the 180th minute time point: SUV_{max}: 1.41 ± 0.14; 1.85 ± 0.19). Conversely, in the study of Kálmán-Szabó *et al.*, the tumor accumulation of [^{61}Cu]Cu-KFTG-NAPamide significantly increased from 30-60 min post injection, then at later time points no remarkable change could be identified (SUV_{mean}: 0.4 ± 0.1; 0.7 ± 0.1; 0.8 ± 0.1; 0.8 ± 0.2; and SUV_{max}: 0.6 ± 0.1; 1.3 ± 0.1; 1.3 ± 0.2; 1.3 ± 0.1 at 30, 60, 90, and 180 min post injection; respectively.[17] Although not yet fully elaborated, we hypothesize that the addition of the acetate group to the chelator could be responsible for the difference between the uptake kinetics of the two probes. Despite the fact using both KFTG and KFTGdiac-based radiopharmaceuticals, the B16F10 tumors could be definitely identified, approximately 2 times higher SUV_{max} values were measured with the [^{61}Cu]Cu-KFTGdiac-NAPamide compound.[17]

In contrast to the unblocked tumors, significantly lower SUV values were registered in case of the α-MSH blocked tumors ($p \leq 0.01$) at all time points that also indicated the receptor specificity of the [^{61}Cu]Cu-KFTGdiac-NAPamide probe (Figure 5, Panel C). Corresponding to our observation, Nagy *et al.* recorded 10-to-15 times lower [^{44}Sc]Sc-DOTA-NAPamide and

[^{68}Ga]Ga-DOTA-NAPamide uptake in the α-MSH pretreated B16F10-carrying mice compared to the unblocked animal cohort.[12]

In addition, a sharp rise in the tumor-to-muscle (T/M) ratio was detected over time that was due to the wash-out of the radiopharmaceutical from the non-target tissues/organs (Figure 5, Panel D), and this corresponded to the findings on [^{61}Cu]Cu-KFTG-NAPamide.[17] Compared to [^{61}Cu]Cu-KFTG-NAPamide, however, the tumor-to-non target ratios observed for [^{61}Cu]Cu-KFTGdiac-NAPamide radiotracer were lower – except for the value measured at the 30 min time point - that could be due to the chemical differences between the two tracers (T/M SUV_{mean}/SUV_{max} for [^{61}Cu]Cu-KFTG-NAPamide: 1.77 ± 0.59 / 2.02 ± 0.23; 6.13 ± 1.15 / 5.61 ± 0.98; 10.17 ± 1.89 / 9.95 ± 1.57; 15.12 ± 1.99 / 13.52 ± 2.08 at 30, 60, 90 and 180 min post injection; respectively and T/M SUV_{mean}/SUV_{max} 3.13 ± 1.05 / 2.92 ± 0.35; 5.84 ± 1.24 / 5.09 ± 0.68; 9.50 ± 1.27 / 7.98 ± 1.09; 12.96 ± 1.35 / 10.65 ± 1.24 for [^{61}Cu]Cu-KFTGdiac-NAPamide at 30, 60, 90 and 180 min post injection, respectively.[17] The quantitative PET parameters are summarized in Table 1.

Table 1. *In vivo* accumulation of [^{61}Cu]Cu-KFTGdiac-NAPamide in subcutaneously growing B16F10 tumors at 30, 60, 90 and 180 min post injection and 9 ± 1 days after tumor induction. Significance level between blocked and non-blocked tumors: $p \leq 0.01$ (**). 200 μg α-MSH was used for blocking.

B16F10 tumor	**[^{61}Cu]Cu-KFTGdiac-NAPamide**			
	30 min	**60 min**	**90 min**	**180 min**
SUVmean	2.03 ± 0.24	1.75 ± 0.17	1.71 ± 0.12	1.41 ± 0.14
SUVmax	2.54 ± 0.31	2.34 ± 0.16	2.24 ± 0.15	1.85 ± 0.19
SUVmean blocked	0.41 ± 0.12**	0.28 ± 0.09**	0.26 ± 0.04**	0.24 ± 0.09**
SUVmax blocked	0.55 ± 0.11**	0.47 ± 0.08**	0.45 ± 0.11**	0.37 ± 0.09**
T/M (SUVmean)	3.13 ± 1.05	5.84 ± 1.24	9.50 ± 1.27	12.69 ± 1.35
T/M (SUVmax)	2.92 ± 0.35	5.09 ± 0.68	7.98 ± 1.09	10.65 ± 1.24
T/M (SUVmean) blocked	1.02 ± 0.12**	1.11 ± 0.21**	1.09 ± 0.08**	1.21 ± 0.14**
T/M (SUVmax) blocked	1.12 ± 0.10**	1.09 ± 0.14**	1.23 ± 0.20**	1.35 ± 0.13**

2.6. Post imaging organ distribution studies

The biodistribution of [^{61}Cu]Cu-KFTGdiac-NAPamide is shown in Figure 6 and Table 2. To obtain information on the pharmacokinetics and organ uptake of [^{61}Cu]Cu-KFTGdiac-NAPamide, *ex vivo* biodistribution studies were carried out in B16F10 xenotransplanted C57BL/6 mice 30, 60, 90 and 180 min after the intravenous administration of the radiotracer.

After dissection, the accumulated activities of the extracted organs and tissues were assessed by a gamma counter.

Based on the *ex vivo* data, the radiopharmaceutical uptake of the brain, lung, stomach, pancreas, salivary glands, bone, muscle and fat tissue remained at minimal level throughout the whole examination. Impeding the entrance of the probe to the central nervous system, the physiological barrier function of the blood-brain barrier may be responsible for the negligible cerebral activity. We suppose that factors in association with the radiotracer metabolism may suggest some explanation for the faint activity of the pancreas and the stomach. Investigating the uptake profile of ^{44}Sc and ^{68}Ga-labelled NAPamide compounds in healthy C57BL/6 mice, Nagy and colleagues reported discrete cerebral, muscular and pulmonary radioactivity, and this was consistent with the current findings.[12] Identically, [^{213}Bi]Bi-DOTA-NAPamide also exhibited faint accumulation 90 min post tracer application in the stomach, lungs and in the muscle tissue of mice with B16F10 melanoma tumors.[30]

As demonstrated by Figure 6, [^{61}Cu]Cu-KFTGdiac-NAPamide displayed relatively higher blood retention with %ID/g values of 1.48 ± 0.44, 1.05 ± 0.22, 0.78 ± 0.21, and 0.44 ± 0.15, 30, 60, 90 and 180 min post-injection; respectively. Similarly, other blood pool organs such as the heart and the spleen also showed moderate tracer accretion ranging from 0.46 ± 0.15 to 1.00 ± 0.34 %ID/g (Table 2). We suppose the role of the lienal reticuloendothelial cells (RES) behind the elevated uptake of the spleen. In line with our results, Kálmán-Szabó and Képes et al. registered moderate ^{213}Bi-labelled DOTA-NAPamide accumulation in the spleen, however, the cardiac and the blood pool radioactivity was rather insignificant in their study.[15] Discrepancies between previous reports and the current research could be attributed to the physicochemical properties of the radiometals (^{213}Bi and ^{61}Cu) or the chemical structure of the applied chelator (DOTA and KFTGdiac).

The highest residence time was found in the liver, the kidneys, the small and the large intestines, the gall bladder and the B16F10 tumors (Figure 6 and Table 2). The increased hepatic, intestinal and renal uptake indicated that the metabolites of the radiotracer were eliminated both via the urinary and the gastrointestinal (GIT) system, that was in accordance with the *logP* value (*logP:* -1.43). Similarly, prior findings on a NAPamide molecule labelled with Lutetium-177 ([^{177}Lu]Lu-DOTA-IPB-NAPamide) also underpinned the role of both the renal and GIT system in probe clearance.[31] In addition, the activity of the RES cells as well as various metabolism-related factors could also be accountable for the experienced outstanding [^{61}Cu]Cu-KFTGdiac-NAPamide uptake of the liver (5.04 ± 0.41, 6.71 ± 0.34, 4.03 ± 0.41 and 3.58 ± 0.44 at 30, 60, 90 and 180 minutes after the injection, respectively). The meaningful

kidney and GIT accumulation coupled with faint blood activities from the early time points and high tracer concentration in the urine evidenced the rapid clearance of [^{61}Cu]Cu-KFTGdiac-NAPamide.

In accordance with our results, other NAPamide-based compounds radiolabelled with Bismuth-205/206 ([$^{205/206}$Bi]Bi-DOTA-IPB-NAPamide)[31] or Fluorine-18 ([^{18}F]F-FB-NAPamide)[14] also exhibited elevated hepatic accumulation and related hepatobiliary way of excretion. Moreover, investigating the imaging behaviour of another MC1-R specific radiopharmaceutical - [^{213}Bi]Bi-DOTA-FOLDamide - Kálmán-Szabó and co-workers reported meaningful liver uptake, that also correlated with the present findings.[15] On the contrary, the negative *logP* values (-1.99) of [^{61}Cu]Cu-KFTG-NAPamide, however, indicated that the clearance of the tracer occurred exclusively through the renal system.[17] Comparing the partition coefficients of the KFTG (*logP:* -1.99) and KFTGdiac-chelated (*logP:* -1.43) molecules, [^{61}Cu]Cu-KFTGdiac-NAPamide was less hydrophilic, that could explain the reason behind why we experienced gastrointestinal elimination besides urinary excretion. Moreover, high renal and bladder uptake of NAPamide molecules labelled with ^{68}Ga or ^{44}Sc also underpinned the unique role of the kidneys in tracer elimination.[12,30].

In line with the *in vivo* data, the high [^{61}Cu]Cu-KFTGdiac-NAPamide retention in the B16F10 tumors further verified the MC1-R pos. tumor-homing ability of the probe. While the tumor accumulation of the KFTGdiac-based radiotracer ([^{61}Cu]Cu-KFTGdiac-NAPamide) reached the maximum already 30 min post tracer administration (6.64 ± 0.34 %ID/g), the highest %ID/g values for [^{61}Cu]Cu-KFTG-NAPamide (7.6 ± 1.7 %ID/g)[17] could be observed at the 2nd measurement point, 60 min post injection (Figure 6, Table 2). On the contrary, the blocked B16F10 tumors barely showed any radioactivity (Table 2), that also corresponded to the *in vivo* findings. Although the tumor uptake decreased gradually over the examination period with 6.64 ± 0.34, 4.21 ± 0.50, 2.88 ± 0.27 and 1.76 ± 0.31 %ID/g present in the neoplastic lesions at 30, 60, 90 and 180 min post injection, relatively higher tumor accumulation in comparison with the background tissues/organs even at later time points led to improved tumor-to-off-target ratios. The higher the T/M ratios are, the better the image contrast is, that ensures the accurate delineation of the pathological lesions from the healthy tissues (T/M ratios: 22.1, 18.3, 18, 17.6 at 30, 60, 90 and 180 min, respectively). The fact that the complex reaches high T/M ratio after 30 minutes, which is slightly reduced in 2 h time window, shows that, the examination time can be reduced significantly with the use of [^{61}Cu]Cu-KFTGdiac-NAPamide tracer, which is advantageous for clinical use. Furthermore, by analyzing the results of previous *ex vivo* studies, it can be concluded that although the accumulation of [^{61}Cu]Cu-KFTGdiac-

NAPamide in B16F10 experimental tumors is somewhat lower than the uptake of [^{61}Cu]Cu-KFTG-NAPamide after 30 or 60 min incubation time,[17] this %ID/g value is still higher than that of ^{64}Cu-, ^{68}Ga- and ^{44}Sc-labeled DOTA-NAPamide probes,[12,16,32] furthermore our radiotracer reaches high T/M ratio 30 min after the *i.v.* administration.

Finally, presumably due to the differences between the chemical structures of the KFTG and KFTGdiac containing radiotracers, a gradual decline of [^{61}Cu]Cu-KFTG-NAPamide uptake was observed for all investigated healthy organs from 30-180 min post tracer application .[17] The major characteristics of [^{61}Cu]Cu-KFTG-NAPamide and [^{61}Cu]Cu-KFTGdiac-NAPamide are summarized in Table 3.

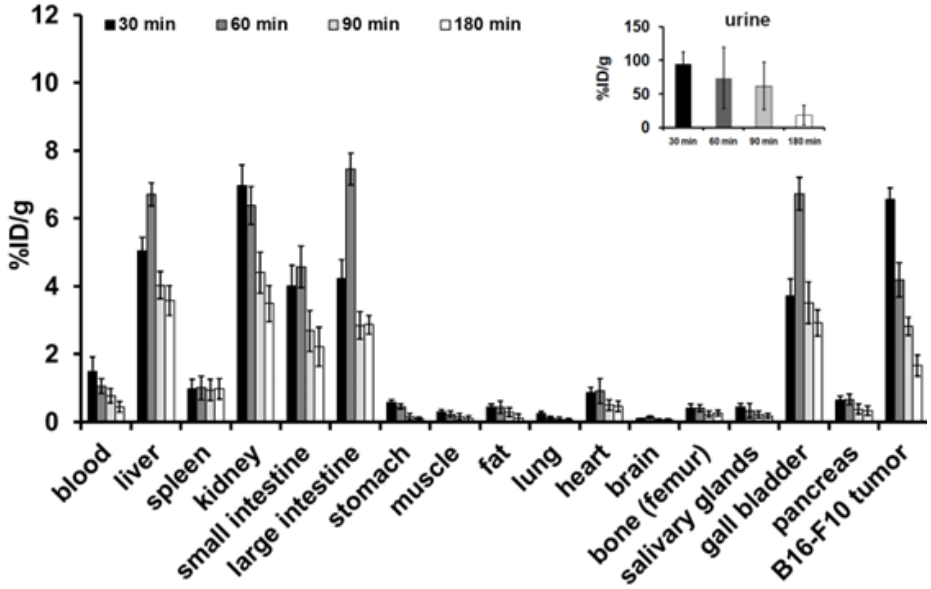

Figure 6. Organ/Tissue uptake of [^{61}Cu]Cu-KFTGdiac-NAPamide. Figure 6 presents the organ distribution of 10.24 ± 1.09 MBq of [^{61}Cu]Cu-KFTGdiac-NAPamide in B16F10 melanoma tumor-bearing C57BL/6 mice. The *ex vivo* uptake pattern was investigated after dissection, 30, 60, 90 and 180 min post intravenous injection of the radiotracer. (n = 5 animals/time point) %ID/g values are presented as mean ± SD.

Table 2. Quantitative analysis of organ/tissue uptake of [^{61}Cu]Cu-KFTGdiac-NAPamide. Table 2 exhibits the uptake values (expressed in %ID/g) of the B16F10 melanoma tumors and other assessed tissues/organs. The *ex vivo* accumulation values were measured after dissection and 30, 60, 90 and 180 min post intravenous injection of the radiotracer. (n = 5 animals/time point) %ID/g values are presented as mean ± SD.

	30 min		**60 min**		**90 min**		**180 min**	
Organ	**%ID/g**	**%ID/g** (T/organ)	**%ID/g**	**%ID/g** (T/organ)	**%ID/g**	**%ID/g** (T/organ)	**%ID/g**	**%ID/g** (T/organ)
blood	1.48 ± 0.44	4.49 ± 0.61	1.05 ± 0.22	4.00 ± 0.58	0.78 ± 0.21	3.69 ± 0.87	0.44 ± 0.15	3.96 ± 1.06
liver	5.04 ± 0.41	1.32 ± 0.12	6.71 ± 0.34	0.63 ± 0.11	4.03 ± 0.41	0.71 ± 0.21	3.58 ± 0.44	0.49 ± 0.07
spleen	0.98 ± 0.27	6.79 ± 1.31	1.00 ± 0.34	4.19 ± 0.99	0.94 ± 0.31	3.05 ± 0.83	0.97 ± 0.31	1.81 ± 0.36
kidney	6.96 ± 0.62	0.95 ± 0.14	6.39 ± 0.56	0.66 ± 0.10	4.40 ± 0.60	0.65 ± 0.11	3.49 ± 0.52	0.50 ± 0.07
small intestine	4.02 ± 0.61	1.65 ± 0.37	4.57 ± 0.62	0.92 ± 0.27	2.68 ± 0.61	1.07 ± 0.12	2.21 ± 0.58	0.80 ± 0.19
large intestine	4.22 ± 0.56	1.57 ± 0.17	7.46 ± 0.46	0.56 ± 0.16	2.85 ± 0.41	1.01 ± 0.12	2.87 ± 0.28	0.61 ± 0.10
stomach	0.57 ± 0.08	11.65 ± 2.49	0.45 ± 0.07	9.36 ± 1.37	0.16 ± 0.09	18.00 ± 2.39	0.10 ± 0.04	17.60 ± 2.37
muscle	0.30 ± 0.07	22.21 ± 3.74	0.23 ± 0.09	18.16 ± 2.87	0.16 ± 0.09	17.59 ± 3.06	0.10 ± 0.09	18.27 ± 3.06
fat	0.44 ± 0.10	15.14 ± 3.41	0.44 ± 0.18	9.63 ± 2.08	0.29 ± 0.12	9.91 ± 1.44	0.12 ± 0.12	15.28 ± 2.33
lung	0.24 ± 0.07	27.67 ± 4.84	0.12 ± 0.04	35.08 ± 6.70	0.09 ± 0.06	32.00 ± 4.93	0.07 ± 0.04	25.14 ± 4.20
heart	0.86 ± 0.16	7.69 ± 1.34	0.91 ± 0.37	4.61 ± 0.99	0.50 ± 0.15	5.72 ± 1.07	0.46 ± 0.15	3.80 ± 0.96
brain	0.10 ± 0.02	65.28 ± 12.09	0.15 ± 0.04	28.94 ± 4.06	0.07 ± 0.02	43.92 ± 7.55	0.06 ± 0.02	27.67 ± 5.04
bone (femur)	0.42 ± 0.11	15.91±3.67	0.41 ± 0.10	10.21 ± 1.31	0.23 ± 0.09	12.37 ± 2.47	0.26 ± 0.09	6.67 ± 1.31
salivary glands	0.45 ± 0.10	14.76±2.48	0.34 ± 0.21	12.38 ± 2.07	0.22 ± 0.10	13.09 ± 2.63	0.18 ± 0.08	9.78 ± 1.46
gall bladder	3.72 ± 0.50	1.78 ± 0.38	6.73 ± 0.49	0.63 ± 0.11	3.51 ± 0.61	0.82 ± 0.21	2.93 ± 0.38	0.60 ± 0.11
pancreas	0.65 ± 0.12	10.23 ± 1.81	0.67 ± 0.15	6.26 ± 1.07	0.38 ± 0.14	7.57 ± 1.08	0.33 ± 0.14	5.28 ± 0.99
B16-F10 tumor	6.64 ± 0.34	-	4.21 ± 0.50	-	2.88 ± 0.27	-	1.76 ± 0.31	-
B16-F10 tumor (blocked)	1.11 ± 0.13**	-	0.72 ± 0.11**	-	0.47 ± 0.09**	-	0.25 ± 0.07**	-

Although the above-detailed results may lay the groundwork for the future *in vivo* application of [^{61}Cu]Cu-KFTGdiac-NAPamide, *ex vivo* measurements conducted at more time points could grant more profound information on tracer kinetics and uptake pattern.[33]

Table 3. Comparison of the most important physico-chemical and imaging characteristics of [^{61}Cu]Cu-KFTGdiac-NAPamide and [^{61}Cu]Cu-KFTG-NAPamide

	[Cu(KFTGdiac)]$^{-}$	**[Cu(KFTG)]$^{+}$**
$t_{1/2,form}$ (s)	1.1	155
$t_{1/2,diss}$ (h)	0.31	2.0
IC_{50} (μM)	–	2.3
plasma stability at 37 °C	intact (5 h)	>96% (6 h)
	[^{61}Cu]Cu-KFTGdiac-NAPamide	**[^{61}Cu]Cu-KFTG-NAPamide**
***logP* value**	-1.43	-1.99
hydrophilicity	less hydrophilic	hydrophilic
way of excretion	urinary and gastrointestinal system	urinary system
cell line	MC1-R positive B16F10	
***in vitro* behaviour**	excellent binding ability	
imaging modality	miniPET	
***in vivo* imaging characteristic**	outstanding tumor-targeting potential	
detected cancerous lesion	MC1-R overexpressing B16F10 melanoma	
tumor uptake	gradual decline (30-to-180 min), two times higher SUVmax compared to [^{61}Cu]Cu-KFTG-NAPamide	significant increase (30-to-60 min), then a plateau (until 180 min)
T/M ratios	sharp rise over time	sharp rise over time, higher than the KFTGdiac conjugate
organs with the highest *ex vivo* uptake	kidneys, liver, small and large intestines, gall bladder	kidneys
***ex vivo* tumor accumulation**	excellent, max. 30 min. post injection	excellent, max. 60 min. post injection
***ex vivo* uptake tendency**	variable	gradual decline over time (30-to-180 min)

3. Conclusions

The outcomes of this study shows that, we were able to further improve the outstanding features of the earlier introduced [^{61}Cu]Cu-KFTG-NAPamide PET tracer by incorporating two acetate pendants into the chelator structure. Structural studies on the pristine [Cu(KFTGdiac)]$^{-}$ complex confirmed that one of the acetate pendants coordinates to copper(II) in apical position and the equatorial plane is accommodated by the nitrogen donor atoms of the macrocyclic cavity. The physico-chemical characterization of the complex exhibits fast complex formation reaction (less than 8 seconds at pH = 5.0 and 25 °C) and suitable inertness ($t_{1/2}$ = 18.4 min at 50 °C in 5 M HCl). Furthermore, the dissociation of the [^{61}Cu]Cu-KFTGdiac-NAPamide tracer was investigated in human plasma resulted no loss of activity during 5 hours.

Additionally, the [^{61}Cu]Cu-KFTGdiac-NAPamide presented excellent MC1-R binding capability as well as favourable T/M ratios, suggesting outstanding imaging performance and suitable tracer kinetics for further *in vivo* applications. The most important physico-chemicals and imaging features are summarized in Table 3. Taken together, our findings capitalize on the relevance of this radiopharmaceutical as an attractive MM PET diagnostic probe for future progression from bench to bedside.

4. Materials and Methods

The highest analytical grade chemicals were applied without further purification. The concentration of the $CuCl_2$ (Merck) solution was determined by means of complexometric titrations in which standardized Na_2H_2EDTA (H_4EDTA: ethylenediaminetetraacetic acid) (Merck) solution was used in the presence of murexid indicator.

Resin-bound NAPamide [Ac-Nle-Asp(*t*Bu)-His(Trt)-(D-Phe)-Arg(Pbf)-Trp(Boc)-Gly-Lys-(Rink Amide MBHA resin)] was purchased from CASLO ApS (Lyngby, Denmark). All other reagents were purchased from Sigma-Aldrich. The mass spectra were recorded on a Waters Acquity UPLC Iclass system (Waters, Milford, MA, USA). For the HPLC (high pressure liquid chromatography) system, HPLC-MS grade ACN and deionized water (Milli-Q, 18.2 MΩ cm^{-1}, Merck, Kenilworth, NJ, USA) were used. Semipreparative RP-HPLC and analytical radio-HPLC were conducted using a Waters LC Module 1 HPLC and a Waters 2695 Alliance HPLC system connected to a UV detector and the ATOMKI 120 CsI scintillation detector. Semipreparative RP HPLC was performed using a Luna C18 10 µm (250 × 10 mm) column; solvent A: TFA (*c* = 0.01 M, pH = 3); solvent B: 95% ACN. Analytical HPLC was performed using a Luna C18 3 µm (150 × 4.6 mm) column, solvent A: TFA; solvent B: 95% ACN.

4.1. Synthesis of the ligand

Commercial reagents/solvents purchased from Sigma-Aldrich (St. Louis, MO, USA), Merck KGaA (Darmstadt, Germany) and Tokyo Chemical Industry (Tokyo, Japan) were used without further purification.

The synthetic reactions were followed by using a Waters Alliance 2690 HPLC unit equipped with Waters 996 PDA detector, and a Phenomenex C18(2) 150*4.6 mm 3 micron column (Table S1 and S2). The preparative HPLC separations were carried out with a YL9100 HPLC system (Korea) equipped with YL9101S degasser, YL9110S pump, YL9120S UV/VIS detector, Phenomenex Luna Prep C18(2) 100A 250x21.20 mm 10 micron 00G-4324-P0 column and Sigma-Aldrich CHROMASOLV® Plus solvents. The NMR (nuclear magnetic resonance) measurements were carried out with Bruker Avance II 500 MHz and Bruker Avance Neo 700 MHz spectrometers using deuterated solvents. Heteronuclear ^{1}H-^{13}C HSQC and HMBC experiments were carried out on Bruker Avance Neo 700 MHz spectrometer. Mass spectra were recorded on a maXis II UHR ESI-QTOF MS Bruker instrument in the Laboratory of Instrumental Analysis, Department of Inorganic and Analytical Chemistry at the University of Debrecen. The purity of the final product (KFTGdiac) was >98.0% determined by reverse-phase HPLC with UV−Vis detection at 220 and 260 nm (for more details, see SI). All compounds are >95% pure by HPLC analysis.

4.2. Kinetic experiments

The complex formation of the $[Cu(KFTGdiac)]^{-}$ was investigated at 25 °C in the presence of 0.15 M NaCl ionic strength. The ligand was used in 10 times excess (0.1 mM) to ensure pseudo-first order conditions. The absorbance change was monitored at 310 nm with a Cary 100 Bio UV-vis spectrophotometer. The reactions were carried out in the pH range 3.0 – 4.4 using DMP buffer (1,4-dimethylpiperazine, pK_a = 4.2) in 50 mM concentration.

The inertness of the complexes was investigated in 5.0 M HCl at 50 °C. The absorbance change was monitored at 310 nm with a Cary 100 Bio UV-vis spectrophotometer. The concentration of the complex was 0.1 mM.

4.3. SOD activity measurements

The decomposition of the superoxide anion radical ($O_2^{\bullet-}$) was studied through a xanthine/xanthine oxidase system. This system produces constantly $O_2^{\bullet-}$ which reduces the *para*-nitro blue tetrazonium chloride (NBT) leading to the formation of formazan with

characteristic molar absorptivity at 560 nm. When the [Cu(KFTGdiac)]$^-$ complex is added to this system, the complex prevents the reduction of NBT by $O_2^{\bullet -}$ which consumption can easily be followed by UV-VIS spectroscopy. The assay was carried out in phosphate buffer (pH = 7.7, c = 0.05 M) containing NBT ($5x10^{-5}$ M) and xanthine ($2x10^{-4}$ M). The reaction was initiated by adding an appropriate amount of xanthine oxidase in order to reach the change in absorbance around ΔA_{560nm} = 0.020-0.030 min^{-1}. The reaction was monitored for 480 s; in the first part of the experiment, the blank sample (without any complex) was monitored for 3-4 min, then the [Cu(KFTGdiac)]$^-$ complex was added to the sample and the absorbance was monitored for another 4 min. The obtained absorbance-time data were fitted with linear lines, then the SOD-activity was expressed by the IC_{50} values.

4.4. EPR measurements and DFT calculation

The X-Band CW-EPR spectrum of the [Cu(KFTGdiac)]$^-$ was registered using a Bruker EleXSys E500 spectrometer (microwave frequency 9.4 GHz, microwave power 13 mW, modulation amplitude 5 G, modulation frequency 100 kHz). Frozen solution EPR spectrum was recorded using quartz EPR tube which was submerged in liquid nitrogen at 77 K. 0.2 mL aliquots of the sample were introduced into the quartz EPR tube and 0.05 mL of methanol was added to prevent the crystallization of water. The frozen solution EPR spectrum was simulated using the "epr" software designated by Rockenbauer and Korecz.[34] The anisotropic spectrum was analysed individually by considering axial $\boldsymbol{g}$- and $\boldsymbol{A}$-tensor ($\boldsymbol{I_{Cu}}$ = 3/2). Since a natural $CuCl_2$ was used for the measurements, the spectrum was calculated as the sum of the spectra of ^{63}Cu and ^{65}Cu weighted by their natural abundances.

The geometry of the [Cu(KFTGdiac)]$^-$ complexes were optimized through the Gaussian 09 (Rev. E.01)[35] software package at DFT level of theory. The hybrid Becke three-parameter B3P86 functional was used in this calculation.[36] The relativistic small-core ECPs SDD and LANL2DZ with the corresponding valence basis sets were employed on the copper(II) and the triple-ζ *def2*-TZVP basis set for the main group elements.[37–39] The effect of the solvent was taken into account adopting the Polarizable Continuum Model (PCM)[40] for water. Single point calculations were carried out for the ground state geometry at the same level of theory which represented true minima on the potential energy surface. The ORCA program (v5.0.3)[41] was used to calculate the $\boldsymbol{g}$ and $\boldsymbol{A}$ tensor for copper(II) coupling. In case of copper(II) couplings, the B3LYP functional with the atom-pairwise dispersion correction including the Becke-Johnson damping scheme (B3LYP D3BJ)[42,43] was combined with the core-property basis set (CP(PPP)) for copper(II) and the EPR-III for nitrogen atoms.[44] The calculations of $\boldsymbol{g}$ tensor was carried out

according to the methods published earlier.[45] Briefly, the double hybrid PBE0-DH functional[46] was used and the calculation included relativistic corrections using the ZORA approximation[47,48] with the *def2*-TZVPP basis set for copper(II) and *def2*-TZVP for further elements.

4.5. Isotope production

220-300 MBq ^{61}Cu was produced from 0.25 mm thick natural zinc foil (Sigma Aldrich, 99.999%) irradiated by 15.5 MeV proton beam (30 min., 20 μA) in a GE PETtrace cyclotron. The irradiated zinc foil was dissolved in 2 mL 7 M nitric acid and mixed with 5.4 mL 2.5 M ammonium formate solution. The ^{61}Cu was trapped on a short Cu resin cartridge, while the contaminating gallium isotopes (66-67Ga) were not retained and rinsed off the resin with 10 mL 0.01 M HCl. The retained activity was eluted with 0.5 mL 7 M HCl and evaporated to dryness with nitrogen stream in a heating block. The ^{61}Cu was redissolved in 100 μL 0.01 M HCl.

4.6. Labeling, general procedures

Synthesis of KFTGdiac-NAPamide. A solution of HBTU (7 mg, 0.018 mmol) in anhydrous DMF (dimethylformamide) (2 mL), DIPEA (N,N-diisopropylethylamine, 3 μL, 0.017 mmol) and a solution of *bis*(*t*Bu)-KFTGdiac (5 mg, 0.007 mmol) in anhydrous DMF (2 mL) were added to the protected, resin-bounded NAPamide [Ac-Nle-Asp(*t*Bu)-His(Trt)-(*D*-Phe)-Arg(Pbf)-Trp(Boc)-Gly-Lys-(Rink Amide MBHA resin)] (30 mg, 0.0045 mmol). The mixture was shaken for 6 hours at RT (room temperature) then the resin was washed with anhydrous DMF. The acidic hydrolysis was performed in 95 % TFA (2 mL). After shaking for 4 hours the TFA was evaporated, and the crude peptide derivative was purified by HPLC. For semipreparative RP-HPLC, a Luna C18(2) 100 Å10 μm (250 × 10 mm) column was eluted at a flow rate of 4 mL·min^{-1} using the following solvents: solvent A: 0.1% HCOOH solvent, B: 95% ACN, gradient: 0 min: 100% A, 2 min: 100% A, 32 min: 100% B, 40 min 100% B. The product was collected between 15 and 16 min. After lyophilization, KFTG-NAPamide was obtained as a white powder (1.3 mg, yield: 20 %). HRMS ESI (electrospray ionization high-resolution mass spectrometry) calc. for: $C_{76}H_{109}N_{21}O_{16}$, 786.9259 $[M+H]^{2+}$ and 524.9532 $[M+H]^{3+}$, found: 786.9244 $[M+H]^{2+}$ and 524.9560 $[M+H]^{3+}$.

The ^{61}Cu solution was mixed with 100 μL pH = 5, 1 M HEPES (4-(2-hydroxyethyl)-1-piperazineethanesulfonic acid) buffer and 10 μL 1 mg/ml peptide solution was added. The mixture was heated for 10 min in a 95 °C heating block. Reaction was monitored with radio-

TLC on ITLC-SG (instant thin layer chromatography medium - silica gel) sheets, eluted with ammonium-acetate methanol 1:1. The reaction mixture was diluted with water and loaded to a Waters Light C18 cartridge. After rinsing with water, the product was eluted with 0.6 mL ethanol. The solution was evaporated to complete dryness and redissolved in 100 μL saline.

4.7. Determination of log*P*

A sample of KFTGdiac-NAPamide in pH = 7 HEPES buffer was added to 0.5 mL water and 0.5 mL octanol. The liquids were mixed thoroughly with vortex mixer for several minutes and left to stand. After phase separation 10 μL samples were taken from both phases and counted with a gamma counter. The octanol/water partition coefficient was found to be –1.43.

4.8. Stability

Plasma stability was determined in human plasma at 37 °C. Significant changes in the radiochemical purity were not observed during the 5 h experiment. The values obtained are scattered within the margin of errors.

4.9. Cell lines

The MC1-R pos. murine B16F10 melanoma cell line was purchased from the American Type Culture Collection (CRL-6475™, ATCC, Virginia, USA). B16F10 cell line was cultured in Dulbecco's Modified Eagle's medium (DMEM, Merck Life Science Ltd., Budapest, Hungary) supplemented with 1% (v/v) MEM Non Essential Amino Acid solution (Merck Life Science Ltd., Budapest, Hungary), 1% MEM Vitamins solution (Merck Life Science Ltd., Budapest, Hungary), 10% Fetal Bovine Serum (FBS, GIBCO Life technologies) and 1% Antibiotic and Antimicotic solution (Merck Life Science Ltd., Budapest, Hungary). Cell culturing occurred at 37 °C in a humidified 5% CO_2 atmosphere. To accomplish *in vitro* experiments and tumor induction the cells were used at 85% confluence. Trypan blue exclusion test was applied for the assessment of the viability of the cells that was always higher than 90%.

4.10. *In vitro* Cellular Uptake and Blocking Studies

To carry out cell uptake and blocking studies, B16F10 cells were aliquoted in plastic test tubes at a cell concentration of 1×10^6 mL^{-1}. Then, 0.37 MBq of [^{61}Cu]Cu-KFTGdiac-NAPamide was added to each tube, and the tubes were incubated for 30, 60, 90 and 180 minutes at 37 °C. After incubation, ice-cold PBS (phosphate-buffered saline) was used for the washing of the samples, which was followed by radioactivity determination applying a calibrated gamma

counter (Perkin-Elmer Packard 406 Cobra, Waltham, MA, USA). For the determination of the cellular efflux of [^{61}Cu]Cu-KFTGdiac-NAPamide, B16F10 cells were first incubated in the presence of the radiotracer (at 37 °C for 30, 60, 90 and 180 min) and then washed with gl-PBS (glucose - phosphate-buffered saline) at room temperature. The supernatant was removed by centrifugation and melanoma cells were resuspended in 2 mL 37 °C gl-PBS and further incubated for 10 min at 37 °C. The efflux was terminated by ice-cold PBS. After the washing step (twice with ice cold PBS), the radioactivity of the pellet was measured by using a gamma-counter.

In blocking experiments B16F10 cells were co-incubated with 5 μM of α-MSH ([Nle^4, D-Phe^7]-α-MSH, Sigma-Aldrich) as a blocking ligand and 0.37 MBq of [^{61}Cu]Cu-KFTGdiac-NAPamide.

The decay-corrected radiotracer uptake was presented as counts/(min∗(10^6 cells)) (cpm). We displayed [^{61}Cu]Cu-KFTGdiac-NAPamide uptake as the percentage of the total radioactivity of the radiotracer added to the cells (%ID/10^6 cells). All experiments were conducted in triplicate.

4.11. Animal Housing

Twelve-week-old C57BL/6 male mice (Charles River; Animalab Ltd., Budapest, Hungary; n = 40) kept under standard laboratory conditions were enrolled in the present experiment. The mice were housed in Individually Ventilated Cages (IVC) in a temperature (26 ± 2 °C)-, and humidity (55 ± 10%)-controlled room with a 12-hour light/12-hour dark schedule. Sterile semi-synthetic diet (Akronom Ltd., Budapest, Hungary) and water were administered *ad libitum* for all study mice. All procedures were complied with all applicable sections of the Hungarian Laws as well as the directions and regulations of the European Union. The permission of the Ethics Committee for Animal Experimentation of the University of Debrecen (ethical permission number: 16/2020/DEMÁB) was granted for the accomplishment of the present research. The fulfilment of the 3R policy was among our priorities throughout the whole procedure.

4.12. *In vivo* Tumor Models

For the induction of MC1-R pos. melanoma tumors, C57BL/6 mice were subcutaneously inoculated in the left shoulder area with 4x10^6 B16F10 cultured murine melanoma cells in 120 μL saline (n = 40). Throughout tumor generation isoflurane-assisted anaesthesia was applied (3% isoflurane (Forane, AbbVie, Chicago, IL, USA), 0.4 L/min O_2, and

1.4 L/min N_2O). 9 ± 1 days after tumor induction, the tumors had grown to an average volume of 200 ± 10 mm^3, and the mice were subjected to *in vivo* microPET imaging and *ex vivo* organ distribution studies.

4.13. *In Vivo* Positron Emission Tomography Imaging

The subcutaneously generated tumors were allowed to grow for approximately 10 days to reach the tumor volume of approximately 200 ± 10 mm^3 for microPET imaging. 9 ± 1 days post tumor generation, B16F10 tumor-bearing mice (n = 20) were intravenously administered with 10.24 ± 1.09 MBq of [^{61}Cu]Cu-KFTGdiac-NAPamide through the lateral tail vein and dynamic PET examinations were performed under isoflurane-induced anaesthesia (3% isoflurane (Forane), AbbVie, Budapest, Hungary; OGYI-T-1414/01) using a preclinical MiniPET-II small animal PET device (Division of Nuclear Medicine and Translational Imaging, Department of Medical Imaging, Faculty of Medicine, University of Debrecen).

4.14. PET Data Assessment

For PET image reconstruction, three-dimensional ordered-subsets expectation-maximization algorithm (3D-OSEM) was used. PET data assessment was performed with the application of the BrainCAD image analysis software. Three-dimensional ellipsoidal volume of interests (VOIs) was carefully delineated around the edge of the radioactivity of selected organs on the coronal PET images to determine their radiotracer concentration. The average signal levels in the VOIs were expressed in standardized uptake values (SUVs), including SUV_{mean} and SUV_{max}. SUV (g/mL) was calculated based on the following formula:

$$SUV = [\text{VOI activity (Bq/ml)}]/[\text{injected activity (Bq)/animal weight (g)}] \quad (2)$$

The average radioactivity of the VOI is indicated by SUV_{mean}, while the SUV_{max} value reflects the highest tracer concentration within that volume. Tumor-to-muscle (T/M SUV_{mean} and T/M SUV_{max}) ratios were also registered from the activity of the tumors and the background (muscle).

4.15. *Ex Vivo* Biodistribution Studies

To assess the radiotracer uptake pattern of the tumor-bearing and healthy control mice, *ex vivo* biodistribution experiments were conducted. For post imaging biodistribution studies, 10.24 ± 1.09 MBq of [^{61}Cu]Cu-KFTGdiac-NAPamide was injected intravenously into the

lateral tail vein of both B16F10 transplanted and healthy control mice. The experimental small animals were sacrificed 30, - 60, - 90, - and 180 minutes after tracer administration. Major organs/tissues including the heart, lung, salivary glands, liver, spleen, gall bladder, pancreas, stomach, intestines, kidneys, brain, bone (femur), urine, blood, muscle, fat tissue and the tumors were harvested, weighed wet and measured for radioactivity by γ-counting (Perkin-Elmer Packard 406 Cobra, Waltham, MA, USA). The radioactivity was decay corrected to the time of injection and the biodistribution results were obtained as %ID/g (n = 5/group).

4.16. Blocking experiments

To verify the MC1-R selectivity of the newly constructed probe, the receptor expressing B16F10 xenograft models were co-injected with approximately 10 MBq of [^{61}Cu]Cu-KFTGdiac-NAPamide and 200 µg α-MSH in 100 µL saline (as a blockade, approx. 350-fold of the ^{61}Cu-labelled peptides). After the co-administration of the radiopharmaceutical and the α-MSH, *in vivo* miniPET acquisition and *ex vivo* uptake studies were carried out with the enrolment of 40 animals (20 and 20 for *in vivo* and *ex vivo* blocking experiments; respectively). Data was collected and analyzed using the same methods as described above.

4.17. Statistical Analyses

We accomplished the statistical analyses with the application of MedCalc 18.5 commercial software package (MedCalc 18.5, MedCalc Software, Mariakerke, Belgium). Two-tailed t-tests, two-way ANOVA or Mann-Whitney U-test were used for the determination of statistical differences. The results are shown as the mean ± SD. Changes with $p < 0.05$ were significant, unless otherwise indicated.

Associated content

Supporting Information

Figures and tables with additional data on the synthesis and characterization of the compounds (NMR, HPLC, MS, EPR and DFT) (PDF)

SMILE codes for the macrocyclic ligands and the NAPamide conjugates (CSV)

Author Contributions

The synthesis, purification and NMR characterization of the KFTGdiac ligand and its pristine Cu(II) complex were accomplished by Sz. Bunda, I. Tímári and G. Papp. The kinetic studies

were performed by Sz. Bunda under the guidance of F. K. Kálmán. The ESR measurements and DFT calculations were carried out by N. Lihi and N. V. May. The labeling experiments, conjugation and *in vitro* characterization of [^{61}Cu]Cu-KFTGdiac-NAPamide was achieved by D. Szikra and D. Szücs. The *in vivo* experiments was executed by I. Kálmán-Szabó and J. Szabó Péliné and evaluated by Z. Képes and Gy. Trencsényi. F. K. Kálmán conceived and supervised the project.

Notes

There are no conflicts to declare. The manuscript was written through contributions of all authors. All authors have given approval to the final version of the manuscript.

Acknowledgements

The research was funded by the Hungarian National Research, Development and Innovation Office (FK-134551) project, the New National Excellence Program ÚNKP-23-5 and by the ÚNKP-23-4-II new national excellence program of the ministry for culture and innovation from the source of the national research, development and innovation fund (K.Z.). F. K. K. and N. L. acknowledge financial support of the János Bolyai Research Scholarship of the Hungarian Academy of Sciences. The authors are indebted to KIFÜ for awarding access to resource based in Hungary. The research was supported by the KDP-2021 program of the Ministry for Innovation and Technology from the source of the National Research, Development and Innovation Fund (Gy.T. and I. K-SZ.). This work is also supported by the University of Debrecen Scientific Research Bridging Fund (DETKA).

List of abbreviations

α-MSH, α-melanocyte-stimulating hormone; CW-EPR, continuous-wave electron paramagnetic resonance; DFT, density-functional theory; ECP, effective core potentials; EPR, electron paramagnetic resonance; FOLDamide, Arg-Arg-Gly-Tyr-Nle-Asp-His-D-Phe-Arg-Trp-NH_2; HMBC, heteronuclear multiple bond correlation; HOLDamide, Gly-pTyr-Nle-Asp-His-D-Phe-Arg-Trp-NH_2; HPLC, high pressure liquid chromatography; HPLC-MS, high pressure liquid chromatography-mass spectrometry; HRMS ESI, electrospray ionization high-resolution mass spectrometry; HSQC, heteronuclear single quantum coherence spectroscopy; ID, injected dose; ITLC-SG, instant thin layer chromatography medium - silica gel; IVC, individually ventilated cages; MARSamide, Gly-Tyr-Nle-Asp-His-D-Phe-Arg-Trp-Arg-Arg-NH_2; MC1-R pos., MC1-R positive; MC1-R, melanocortin-1 receptor; MM, malignant

melanoma; MoAb, monoclonal antibodies; NAPamide, Nle-Asp-His-D-Phe-Arg-Trp-Gly-Lys-NH_2; NMR, nuclear magnetic resonance; PCM, polarizable continuum model; PDA, photo diode array; PET, positron emission tomography; RES, reticuloendothelial cells; RP-HPLC, reversed-phase high pressure liquid chromatography; SD, standard deviation; SPECT, single-photon emission computed tomography; SUV, standardized uptake value; T/M ratio, tumor-to-muscle ratio; VOI, volume of interest

References

(1) Davey, M. G.; Miller, N.; McInerney, N. M. A Review of Epidemiology and Cancer Biology of Malignant Melanoma. *Cureus* **2021**. https://doi.org/10.7759/cureus.15087.

(2) Shi, H.; Cheng, Z. MC1R and Melanin-Based Molecular Probes for Theranostic of Melanoma and Beyond. *Acta Pharmacol Sin* **2022**, *43* (12), 3034–3044. https://doi.org/10.1038/s41401-022-00970-y.

(3) Ren, G.; Miao, Z.; Liu, H.; Jiang, L.; Limpa-Amara, N.; Mahmood, A.; Gambhir, S. S.; Cheng, Z. Melanin-Targeted Preclinical PET Imaging of Melanoma Metastasis. *J Nucl Med* **2009**, *50* (10), 1692–1699. https://doi.org/10.2967/jnumed.109.066175.

(4) Greguric, I.; Taylor, S. R.; Denoyer, D.; Ballantyne, P.; Berghofer, P.; Roselt, P.; Pham, T. Q.; Mattner, F.; Bourdier, T.; Neels, O. C.; Dorow, D. S.; Loc'h, C.; Hicks, R. J.; Katsifis, A. Discovery of [^{18} F] *N* -(2-(Diethylamino)Ethyl)-6-Fluoronicotinamide: A Melanoma Positron Emission Tomography Imaging Radiotracer with High Tumor to Body Contrast Ratio and Rapid Renal Clearance. *J. Med. Chem.* **2009**, *52* (17), 5299–5302. https://doi.org/10.1021/jm9008423.

(5) Denoyer, D.; Greguric, I.; Roselt, P.; Neels, O. C.; Aide, N.; Taylor, S. R.; Katsifis, A.; Dorow, D. S.; Hicks, R. J. High-Contrast PET of Melanoma Using ^{18} F-MEL050, a Selective Probe for Melanin with Predominantly Renal Clearance. *J Nucl Med* **2010**, *51* (3), 441–447. https://doi.org/10.2967/jnumed.109.070060.

(6) Divgi, C. R.; Larson, S. M. Radiolabeled Monoclonal Antibodies in the Diagnosis and Treatment of Malignant Melanoma. *Seminars in Nuclear Medicine* **1989**, *19* (4), 252–261. https://doi.org/10.1016/S0001-2998(89)80019-4.

(7) Chakravarty, R.; Chakraborty, S.; Ningthoujam, R. S.; Vimalnath Nair, K. V.; Sharma, K. S.; Ballal, A.; Guleria, A.; Kunwar, A.; Sarma, H. D.; Vatsa, R. K.; Dash, A. Industrial-Scale Synthesis of Intrinsically Radiolabeled ^{64} CuS Nanoparticles for Use in Positron Emission Tomography (PET) Imaging of Cancer. *Ind. Eng. Chem. Res.* **2016**, *55* (48), 12407–12419. https://doi.org/10.1021/acs.iecr.6b03405.

(8) Wolf Horrell, E. M.; Boulanger, M. C.; D'Orazio, J. A. Melanocortin 1 Receptor: Structure, Function, and Regulation. *Front. Genet.* **2016**, *7*. https://doi.org/10.3389/fgene.2016.00095.

(9) Rosenkranz, A. A.; Slastnikova, T. A.; Durymanov, M. O.; Sobolev, A. S. Malignant Melanoma and Melanocortin 1 Receptor. *Biochemistry Moscow* **2013**, *78* (11), 1228–1237. https://doi.org/10.1134/S0006297913110035.

(10) Tatro, J. B.; Atkins, M.; Mier, J. W.; Hardarson, S.; Wolfe, H.; Smith, T.; Entwistle, M. L.; Reichlin, S. Melanotropin Receptors Demonstrated in Situ in Human Melanoma. *J. Clin. Invest.* **1990**, *85* (6), 1825–1832. https://doi.org/10.1172/JCI114642.

(11) Swope, V.; Abdel-Malek, Z. MC1R: Front and Center in the Bright Side of Dark Eumelanin and DNA Repair. *IJMS* **2018**, *19* (9), 2667. https://doi.org/10.3390/ijms19092667.

(12) Nagy, G.; Dénes, N.; Kis, A.; Szabó, J. P.; Berényi, E.; Garai, I.; Bai, P.; Hajdu, I.; Szikra, D.; Trencsényi, G. Preclinical Evaluation of Melanocortin-1 Receptor (MC1-R) Specific 68Ga- and 44Sc-Labeled DOTA-NAPamide in Melanoma Imaging. *European Journal of Pharmaceutical Sciences* **2017**, *106*, 336–344. https://doi.org/10.1016/j.ejps.2017.06.026.
(13) Miao, Y.; Benwell, K.; Quinn, T. P. 99mTc- and 111In-Labeled Alpha-Melanocyte-Stimulating Hormone Peptides as Imaging Probes for Primary and Pulmonary Metastatic Melanoma Detection. *J Nucl Med* **2007**, *48* (1), 73–80.
(14) Cheng, Z.; Zhang, L.; Graves, E.; Xiong, Z.; Dandekar, M.; Chen, X.; Gambhir, S. S. Small-Animal PET of Melanocortin 1 Receptor Expression Using a 18F-Labeled -Melanocyte-Stimulating Hormone Analog. *Journal of Nuclear Medicine* **2007**, *48* (6), 987–994. https://doi.org/10.2967/jnumed.107.039602.
(15) Kálmán-Szabó, I.; Képes, Z.; Fekete, A.; Vágner, A.; Nagy, G.; Szücs, D.; Gyuricza, B.; Arató, V.; Varga, J.; Kárpáti, L.; Garai, I.; Mándity, I.; Bruchertseifer, F.; Elek, J.; Szikra, D.; Trencsényi, G. In Vivo Evaluation of Newly Synthesized 213Bi-Conjugated Alpha-Melanocyte Stimulating Hormone (α-MSH) Peptide Analogues in Melanocortin-1 Receptor (MC1-R) Positive Experimental Melanoma Model. *Journal of Pharmaceutical and Biomedical Analysis* **2023**, *229*, 115374. https://doi.org/10.1016/j.jpba.2023.115374.
(16) Cheng, Z.; Xiong, Z.; Subbarayan, M.; Chen, X.; Gambhir, S. S. ^{64} Cu-Labeled Alpha-Melanocyte-Stimulating Hormone Analog for MicroPET Imaging of Melanocortin 1 Receptor Expression. *Bioconjugate Chem.* **2007**, *18* (3), 765–772. https://doi.org/10.1021/bc060306g.
(17) Kálmán-Szabó, I.; Bunda, S.; Lihi, N.; Szaniszló, Z.; Szikra, D.; Szabó Péliné, J.; Fekete, A.; Gyuricza, B.; Szücs, D.; Papp, G.; Trencsényi, G.; Kálmán, F. K. 61Cu-Labelled Radiodiagnostics of Melanoma with NAPamide-Targeted Radiopharmaceutical. *International Journal of Pharmaceutics* **2023**, *632*, 122527. https://doi.org/10.1016/j.ijpharm.2022.122527.
(18) McCarthy, D. W.; Bass, L. A.; Cutler, P. D.; Shefer, R. E.; Klinkowstein, R. E.; Herrero, P.; Lewis, J. S.; Cutler, C. S.; Anderson, C. J.; Welch, M. J. High Purity Production and Potential Applications of Copper-60 and Copper-61. *Nuclear Medicine and Biology* **1999**, *26* (4), 351–358. https://doi.org/10.1016/S0969-8051(98)00113-9.
(19) Bleuel, D. L.; Bernstein, L. A.; Marsh, R. A.; Morrell, J. T.; Rusnak, B.; Voyles, A. S. Precision Measurement of Relative γ -Ray Intensities from the Decay of 61Cu. *Applied Radiation and Isotopes* **2021**, *170*, 109625. https://doi.org/10.1016/j.apradiso.2021.109625.
(20) Fonseca, A. I.; Alves, V. H.; Do Carmo, S. J. C.; Falcão, A.; Abrunhosa, A. J.; Alves, F. GMP-Automated Purification of Copper-61 Produced in Cyclotron Liquid Targets: Methodological Aspects. *CRP* **2021**, *14* (4), 420–428. https://doi.org/10.2174/1874471013666201112141844.
(21) Williams, H. A.; Robinson, S.; Julyan, P.; Zweit, J.; Hastings, D. A Comparison of PET Imaging Characteristics of Various Copper Radioisotopes. *Eur J Nucl Med Mol Imaging* **2005**, *32* (12), 1473–1480. https://doi.org/10.1007/s00259-005-1906-9.
(22) Hubin, T. Synthesis and Coordination Chemistry of Topologically Constrained Azamacrocycles. *Coordination Chemistry Reviews* **2003**, *241* (1–2), 27–46. https://doi.org/10.1016/S0010-8545(02)00307-7.
(23) Csupász, T.; Lihi, N.; Fekete, Z.; Nagy, A.; Botár, R.; Forgács, V.; Szikra, D.; May, N. V.; Tircsó, G.; Kálmán, F. K. Exceptionally Fast Formation of Stable Rigidified Cross-Bridged Complexes Formed with Cu(II) Isotopes for Molecular Imaging. *Inorg. Chem. Front.* **2022**, *9* (6), 1217–1223. https://doi.org/10.1039/D1QI01526E.

(24) Shircliff, A. D.; Burke, B. P.; Davilla, D. J.; Burgess, G. E.; Okorocha, F. A.; Shrestha, A.; Allbritton, E. M. A.; Nguyen, P. T.; Lamar, R. L.; Jones, D. G.; Gorbet, M.-J.; Allen, M. B.; Eze, J. I.; Fernandez, A. T.; Ramirez, D.; Archibald, S. J.; Prior, T. J.; Krause, J. A.; Oliver, A. G.; Hubin, T. J. An Ethylene Cross-Bridged Pentaazamacrocycle and Its Cu^{2+} Complex: Constrained Ligand Topology and Excellent Kinetic Stability. *Chem. Commun.* **2020**, *56* (54), 7519–7522. https://doi.org/10.1039/D0CC00919A.
(25) Anderson, C. J.; Wadas, T. J.; Wong, E. H.; Weisman, G. R. Cross-Bridged Macrocyclic Chelators for Stable Complexation of Copper Radionuclides for PET Imaging. *Q J Nucl Med Mol Imaging* **2008**, *52* (2), 185–192.
(26) Lacerda, S.; Campello, M. P.; Santos, I. C.; Santos, I.; Delgado, R. Study of the Cyclen Derivative 2-[1,4,7,10-Tetraazacyclododecan-1-Yl]-Ethanethiol and Its Complexation Behaviour towards d-Transition Metal Ions. *Polyhedron* **2007**, *26* (14), 3763–3773. https://doi.org/10.1016/j.poly.2007.04.037.
(27) Breeman, W. A. P.; De Blois, E.; Sze Chan, H.; Konijnenberg, M.; Kwekkeboom, D. J.; Krenning, E. P. 68Ga-Labeled DOTA-Peptides and 68Ga-Labeled Radiopharmaceuticals for Positron Emission Tomography: Current Status of Research, Clinical Applications, and Future Perspectives. *Seminars in Nuclear Medicine* **2011**, *41* (4), 314–321. https://doi.org/10.1053/j.semnuclmed.2011.02.001.
(28) Evans, B. J.; King, A. T.; Katsifis, A.; Matesic, L.; Jamie, J. F. Methods to Enhance the Metabolic Stability of Peptide-Based PET Radiopharmaceuticals. *Molecules* **2020**, *25* (10), 2314. https://doi.org/10.3390/molecules25102314.
(29) Froidevaux, S.; Calame-Christe, M.; Tanner, H.; Eberle, A. N. Melanoma Targeting with DOTA-Alpha-Melanocyte-Stimulating Hormone Analogs: Structural Parameters Affecting Tumor Uptake and Kidney Uptake. *J Nucl Med* **2005**, *46* (5), 887–895.
(30) Csikos, C.; Képes, Z.; Fekete, A.; Vágner, A.; Nagy, G.; Gyuricza, B.; Arató, V.; Kárpáti, L.; Mándity, I.; Bruchertseifer, F.; Halmos, G.; Szikra, D.; Trencsényi, G. Evaluation of the Therapeutic Efficacy of 213Bi-Labelled DOTA-Conjugated Alpha-Melanocyte Stimulating Hormone Peptide Analogues in Melanocortin-1 Receptor Positive Preclinical Melanoma Model. *International Journal of Pharmaceutics* **2023**, *644*, 123344. https://doi.org/10.1016/j.ijpharm.2023.123344.
(31) Szücs, D.; Szabó, J. P.; Arató, V.; Gyuricza, B.; Szikra, D.; Tóth, I.; Képes, Z.; Trencsényi, G.; Fekete, A. Investigation of the Effect on the Albumin Binding Moiety for the Pharmacokinetic Properties of 68Ga-, 205/206Bi-, and 177Lu-Labeled NAPamide-Based Radiopharmaceuticals. *Pharmaceuticals* **2023**, *16* (9), 1280. https://doi.org/10.3390/ph16091280.
(32) Zhang, C.; Lin, K.-S.; Bénard, F. Molecular Imaging and Radionuclide Therapy of Melanoma Targeting the Melanocortin 1 Receptor. *Mol Imaging* **2017**, *16*, 153601211773791. https://doi.org/10.1177/1536012117737919.
(33) Miao, Y.; Owen, N. K.; Whitener, D.; Gallazzi, F.; Hoffman, T. J.; Quinn, T. P. *In Vivo* Evaluation of ^{188} Re-labeled Alpha-melanocyte Stimulating Hormone Peptide Analogs for Melanoma Therapy. *Intl Journal of Cancer* **2002**, *101* (5), 480–487. https://doi.org/10.1002/ijc.10640.
(34) Rockenbauer, A.; Korecz, L. Automatic Computer Simulations of ESR Spectra. *Appl. Magn. Reson.* **1996**, *10* (1–3), 29–43. https://doi.org/10.1007/BF03163097.
(35) Frisch, M. J.; Trucks, G. W.; Schlegel, H. B.; Scuseria, G. E.; Robb, M. A.; Cheeseman, J. R.; Scalmani, G.; Barone, V.; Mennucci, B.; Petersson, G. A.; Nakatsuji, H.; Caricato, M.; Li, X.; Hratchian, H. P.; Izmaylov, A. F.; Bloino, J.; Zheng, G.; Sonnenberg, J. L.; Hada, M.; Ehara, M.; Toyota, K.; Fukuda, R.; Hasegawa, J.; Ishida, M.; Nakajima, T.; Honda, Y.; Kitao, O.; Nakai, H.; Vreven, T.; Montgomery Jr., J. A.; Peralta, J. E.; Ogliaro, F.; Bearpark, M. J.; Heyd, J.; Brothers, E. N.; Kudin, K. N.; Staroverov, V. N.;

Kobayashi, R.; Normand, J.; Raghavachari, K.; Rendell, A. P.; Burant, J. C.; Iyengar, S. S.; Tomasi, J.; Cossi, M.; Rega, N.; Millam, N. J.; Klene, M.; Knox, J. E.; Cross, J. B.; Bakken, V.; Adamo, C.; Jaramillo, J.; Gomperts, R.; Stratmann, R. E.; Yazyev, O.; Austin, A. J.; Cammi, R.; Pomelli, C.; Ochterski, J. W.; Martin, R. L.; Morokuma, K.; Zakrzewski, V. G.; Voth, G. A.; Salvador, P.; Dannenberg, J. J.; Dapprich, S.; Daniels, A. D.; Farkas, Ö.; Foresman, J. B.; Ortiz, J. V.; Cioslowski, J.; Fox, D. J. Gaussian 09, Gaussian, Inc.: Wallingford, CT, USA, 2009. .

(36) Becke, A. D. Density-functional Thermochemistry. III. The Role of Exact Exchange. *The Journal of Chemical Physics* **1993**, *98* (7), 5648–5652. https://doi.org/10.1063/1.464913.

(37) Dolg, M.; Wedig, U.; Stoll, H.; Preuss, H. Energy-adjusted *a b i n i t i o* Pseudopotentials for the First Row Transition Elements. *The Journal of Chemical Physics* **1987**, *86* (2), 866–872. https://doi.org/10.1063/1.452288.

(38) Bühl, M.; Kabrede, H. Geometries of Transition-Metal Complexes from Density-Functional Theory. *J. Chem. Theory Comput.* **2006**, *2* (5), 1282–1290. https://doi.org/10.1021/ct6001187.

(39) Hay, P. J.; Wadt, W. R. *Ab Initio* Effective Core Potentials for Molecular Calculations. Potentials for K to Au Including the Outermost Core Orbitals. *The Journal of Chemical Physics* **1985**, *82* (1), 299–310. https://doi.org/10.1063/1.448975.

(40) Tomasi, J.; Mennucci, B.; Cammi, R. Quantum Mechanical Continuum Solvation Models. *Chem. Rev.* **2005**, *105* (8), 2999–3094. https://doi.org/10.1021/cr9904009.

(41) Neese, F. The ORCA Program System. *WIREs Comput Mol Sci* **2012**, *2* (1), 73–78. https://doi.org/10.1002/wcms.81.

(42) Grimme, S.; Ehrlich, S.; Goerigk, L. Effect of the Damping Function in Dispersion Corrected Density Functional Theory. *J Comput Chem* **2011**, *32* (7), 1456–1465. https://doi.org/10.1002/jcc.21759.

(43) Grimme, S.; Antony, J.; Ehrlich, S.; Krieg, H. A Consistent and Accurate *Ab Initio* Parametrization of Density Functional Dispersion Correction (DFT-D) for the 94 Elements H-Pu. *The Journal of Chemical Physics* **2010**, *132* (15), 154104. https://doi.org/10.1063/1.3382344.

(44) Rega, N.; Cossi, M.; Barone, V. Development and Validation of Reliable Quantum Mechanical Approaches for the Study of Free Radicals in Solution. *The Journal of Chemical Physics* **1996**, *105* (24), 11060–11067. https://doi.org/10.1063/1.472906.

(45) Zimmeter, K.; Vileno, B.; Platas-Iglesias, C.; Vinjamuri, B.; Sour, A.; Faller, P. Derivatization of the Peptidic Xxx-Zzz-His Motif toward a Ligand with Attomolar Cu^{II} Affinity under Maintaining High Selectivity and Fast Redox Silencing. *Inorg. Chem.* **2023**, *62* (24), 9429–9439. https://doi.org/10.1021/acs.inorgchem.3c00480.

(46) Brémond, E.; Adamo, C. Seeking for Parameter-Free Double-Hybrid Functionals: The PBE0-DH Model. *The Journal of Chemical Physics* **2011**, *135* (2), 024106. https://doi.org/10.1063/1.3604569.

(47) Lenthe, E. V.; Baerends, E. J.; Snijders, J. G. Relativistic Regular Two-Component Hamiltonians. *The Journal of Chemical Physics* **1993**, *99* (6), 4597–4610. https://doi.org/10.1063/1.466059.

(48) Van Lenthe, E.; Baerends, E. J.; Snijders, J. G. Relativistic Total Energy Using Regular Approximations. *The Journal of Chemical Physics* **1994**, *101* (11), 9783–9792. https://doi.org/10.1063/1.467943.

TOC

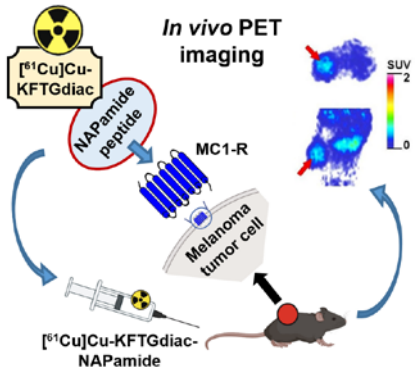
[61Cu]Cu-KFTGdiac
NAPamide peptide
In vivo PET imaging
SUV
2
0
MC1-R
Melanoma tumor cell
[61Cu]Cu-KFTGdiac-NAPamide